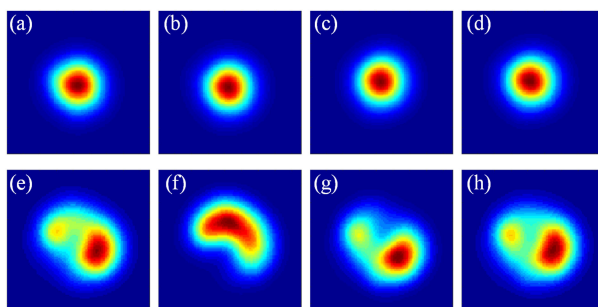


# Investigating the Performance of a Few-Mode Fiber for Distributed Acoustic Sensing






Volume 11, Number 5, October 2019

Yuan Mao, *Senior Member, IEEE*  
Islam Ashry, *Senior Member, IEEE*  
Mohd Sharizal Alias, *Senior Member, IEEE*  
Tien Khee Ng, *Senior Member, IEEE*  
Frode Hveding  
Muhammad Arsalan  
Boon Siew Ooi, *Senior Member, IEEE*



DOI: 10.1109/JPHOT.2019.2940951

# Investigating the Performance of a Few-Mode Fiber for Distributed Acoustic Sensing

Yuan Mao,<sup>1</sup> *Senior Member, IEEE*,  
Islam Ashry ,<sup>1</sup> *Senior Member, IEEE*,  
Mohd Sharizal Alias ,<sup>1</sup> *Senior Member, IEEE*,  
Tien Khee Ng ,<sup>1</sup> *Senior Member, IEEE*, Frode Hveding,<sup>2</sup>  
Muhammad Arsalan ,<sup>2</sup>  
and Boon Siew Ooi ,<sup>1</sup> *Senior Member, IEEE*

<sup>1</sup>Computer, Electrical, and Mathematical Sciences and Engineering, King Abdullah University of Science and Technology, Thuwal 23955-6900, Saudi Arabia

<sup>2</sup>EXPEC Advance Research Center–Saudi Aramco, Dhahran 34465, Saudi Arabia

DOI:10.1109/JPHOT.2019.2940951

This work is licensed under a Creative Commons Attribution 4.0 License. For more information, see <https://creativecommons.org/licenses/by/4.0/>

Manuscript received July 14, 2019; revised August 21, 2019; accepted September 9, 2019. Date of publication September 16, 2019; date of current version October 4, 2019. This work was supported in part by Saudi Aramco under Grant RGC/3/3138-01, in part by the King Abdullah University of Science and Technology (KAUST) baseline funding under Grant BAS/1/1614-01-01, and in part by KAUST equipment funding under Grants KCR/1/2081-01-01 and GEN/1/6607-01-01. (Yuan Mao and Islam Ashry contributed equally to this work.) Corresponding author: Boon S. Ooi (e-mail: boon.ooi@kaust.edu.sa)

**Abstract:** We experimentally investigated the performance of a distributed acoustic sensor (DAS) designed using a few-mode fiber (FMF), when launching different spatial modes under intentional index perturbation within the fiber. Our demonstration showed that the quasi-single mode (QSM) operated FMF offers higher signal-to-noise ratio (SNR) for the DAS, compared with the case when launching other degenerate higher order modes. Additionally, we compared the behavior of the single-mode fiber (SMF)- and FMF-based DAS when using optical pulses of varying power levels. The FMF enables the realization of a DAS with longer sensing range and higher spatial resolution. The developed FMF-based DAS is further tested via sensing various vibration events produced by piezoelectric transducer (PZT) cylinder, pencil break, and loudspeaker.

**Index Terms:** Acoustic sensors, optical fiber sensors, optical fibers, optical sensors.

## 1. Introduction

The recent development of few-mode fibers (FMFs) has impacted on many potential applications [1]–[5]. In optical communications, for example, the implementation of mode division multiplexing (MDM) in a FMF-based network can significantly enhance its overall data capacity by utilizing individual linearly-polarized (LP) modes as distinct communication channels [1]–[3]. Optical sensing has also benefited from the advances in FMFs via primarily two different approaches. The underlying principle of one approach relies on the observation that different LP modes react differently to perturbations produced by external parameters such as strain, temperature, gas, etc. Therefore, by monitoring responses of different LP modes, one can simultaneously measure multiple parameters or develop new sensing mechanisms. For instance, writing fiber Bragg grating (FBG) in FMFs has been employed to simultaneously measure temperature and refractive index

(RI) [6], temperature and strain [7], and bending and strain [8]. In other trials, mode dependent loss in FMFs has been utilized to design extremely large scale absorption-based sensing network [9] and to reconstruct spatial distributions of chemicals that diffuse into a FMF [10], functionalities which are almost impossible to implement using conventional single-mode fiber (SMF) based sensors. In another approach, researchers use FMF as a compromise between SMF and multimode fiber (MMF) to develop optical sensors with a high signal-to-noise ratio (SNR) [11]. This is because FMF supports higher threshold power of nonlinearity, compared with the standard SMF, and mitigates the modal dispersion effect that exists in the traditional MMF.

Since distributed optical fiber sensors have been widely used in a myriad of industrial applications, such as oil and gas production [12] and real-time structural health monitoring [13], and because of the unique characteristics of FMFs, investigating the performance of such sensors with FMFs has recently attracted considerable research interest. For example, Brillouin optical time-domain reflectometry (BOTDR) developed using a two-mode fiber (TMF) can offer simultaneous distributed temperature and strain measurements [14]. Another trial by Wang *et al.* reported a TMF-based Raman distributed temperature sensor (DTS) having a 20 km sensing range which is twice that of the conventional MMF-based DTS [11]. Furthermore, FMFs allow combining two different distributed optical fiber sensors in a single platform, such as developing a hybrid Raman-Brillouin system for simultaneous distributed curvature and temperature sensing [15]. Although the importance of the Rayleigh distributed acoustic sensor (DAS) designed using the phase-sensitive optical time domain reflectometry ( $\Phi$ -OTDR) [16], its performance with FMFs has not been thoroughly explored. In particular, Mengmeng *et al.* combined the Rayleigh signals of different spatial modes within a TMF to improve the SNR of the reported DAS [17].

In real applications, a FMF might be subjected to a relatively strong refractive-index perturbation which induces intermodal coupling. To the best of our knowledge, the performance of the FMF-based DAS has not been investigated when injecting different spatial modes in the presence of index perturbation within the fiber. Additionally, it is worth exploring the performance of the FMF-based DAS when launching pump pulses with power levels higher than the standard SMF's threshold power of nonlinearity. This is important to validate the possibility of using a FMF for upgrading the conventional DAS system's sensing range and spatial resolution.

In this paper, we investigate the performance of an  $\Phi$ -OTDR-based DAS designed using a TMF. The SNR of the DAS is monitored when injecting the  $LP_{01}$ ,  $LP_{11a}$ , and  $LP_{11b}$  modes into the TMF while an index perturbation is intentionally applied on the fiber to induce intermodal coupling. We further compare the Rayleigh signal profiles and SNR of the SMF- and TMF-based DAS when launching pulses of different power levels. The results show that, with careful selection of the TMF type, the quasi-single mode (QSM) operated TMF can improve the sensing range and spatial resolution of DAS with acceptable SNR. The work presented here paves the way for integrating DAS with the other optical fiber distributed sensors that utilize MMF, such as DTS.

## 2. Mode-Dependent SNR of the TMF-Based DAS

In this section, we explore the SNR-dependency of the TMF-based DAS on the type of the input spatial mode, when we deliberately induce intermodal coupling within the TMF. The experimental setup of the used optical fiber DAS is shown in Fig. 1(a). A narrow linewidth laser source generates a continuous wave (CW) light of 16 dBm optical power, 100 Hz linewidth, and 1535 nm operation wavelength. The laser light is modulated by an acousto-optic modulator (AOM) to produce optical pulses with 20 kHz repetition rate and 100 ns width offering 10 m sensing spatial resolution. The modulated light is amplified by an erbium-doped-fiber-amplifier (EDFA1), and then launched through a circulator into one of the input ports of a  $3 \times 1$  photonic lantern which acts as a mode-division-multiplexer/demultiplexer (MUX/DEMUX). The output port of the photonic lantern is connected to a TMF (YOFC Co., Ltd.) which is a step-index fiber of V-number equals 3.27 at the 1535 nm operation wavelength. Thus, the fiber supports propagating the  $LP_{01}$ ,  $LP_{11a}$ , and  $LP_{11b}$  mode, where the latter two modes are degenerate. The length of the TMF is  $\sim 3.1$  km and we attach a 10 m section of it, near its end, to a piezoelectric transducer (PZT) cylinder such that its vibration frequency

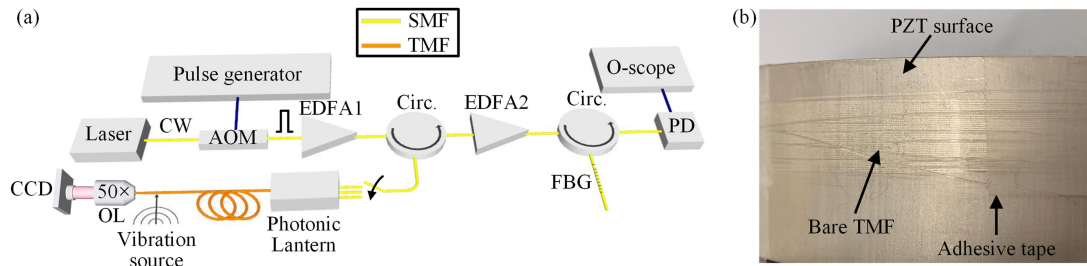


Fig. 1. (a) Experimental schematic of the optical fiber DAS using a TMF. Circ., circulator; O-scope, oscilloscope. (b) Arrangement of winding the used TMF around the PZT cylinder.

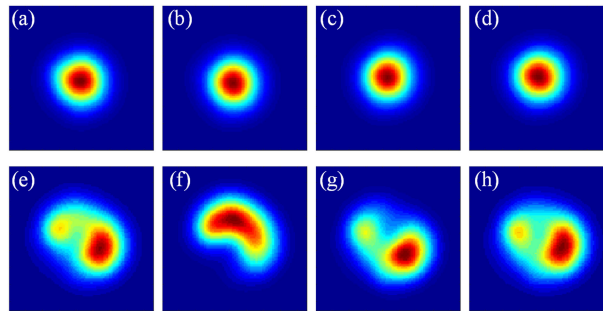


Fig. 2. Temporal changes of the intensity profiles at the TMF output port when injecting the  $LP_{01}$  (a–d) and  $LP_{11a}$  mode (e–h) into the TMF, under index perturbation.

is controllable via a function generator. PZT cylinder is the typical vibration source used for the calibration of  $\Phi$ -OTDR-based DAS [18]. As shown in Fig. 1(b), we wind the bare TMF around the PZT surface and then secure this arrangement with an adhesive tape. At the output end of the TMF, shown in Fig. 1(a), an objective lens ( $50\times$ ,  $NA = 0.45$ ) and a near-infrared CCD camera are used to image the TMF output intensity profile. The backscattered Rayleigh traces from the TMF are recorded through a direct detection scheme. The traces are firstly amplified by another erbium-doped-fiber-amplifier (EDFA2) which amplified spontaneous emission (ASE) noise is filtered out by a FBG. The filtered backscattered Rayleigh traces are then detected by a photodetector (PD) and sampled at 125 MHz rate using an oscilloscope.

We individually inject the  $LP_{01}$ ,  $LP_{11a}$ , and  $LP_{11b}$  mode, using the photonic lantern, into the TMF and collect the Rayleigh traces of the same type as the input mode. To induce intermodal coupling within the fiber, we freely hang a  $\sim 1$  m-section of the TMF to be subjected to an air flow produced by a fan rotating at  $\sim 1100$  rpm speed and positioned at a  $\sim 1$  m-distance from the hanged fiber. The hanged fiber section is located just after the TMF input port and the air flow continuously shakes it to perturb its refractive index. Figs. 2(a–d) and 2(e–h) respectively show representative examples at different time instances to the output beam profiles of the TMF when injecting the  $LP_{01}$  and  $LP_{11a}$  mode, under index perturbation. Since the two degenerate modes ( $LP_{11a}$  and  $LP_{11b}$ ) behave similarly, we present only the results of the  $LP_{11a}$  mode. The fundamental mode preserves its intensity profile at the end of the TMF, even in the presence of index perturbation. This is mainly because the step-index profile of the TMF can significantly suppress the intermodal coupling between the  $LP_{01}$  and  $LP_{11}$  mode [19]. In contrast, the  $LP_{11a}$  mode exhibits obvious intermodal coupling mainly with the  $LP_{11b}$  mode which is expected because the two degenerate modes share the same propagation constant [20].

Under these index perturbation conditions, we record the Rayleigh signals of the same type as the individually injected modes ( $LP_{01}$  and  $LP_{11a}$ ), while the PZT cylinder is vibrating with 500 Hz frequency. Figs. 3(a) and 3(b) show representative examples of 10 consecutive Rayleigh traces

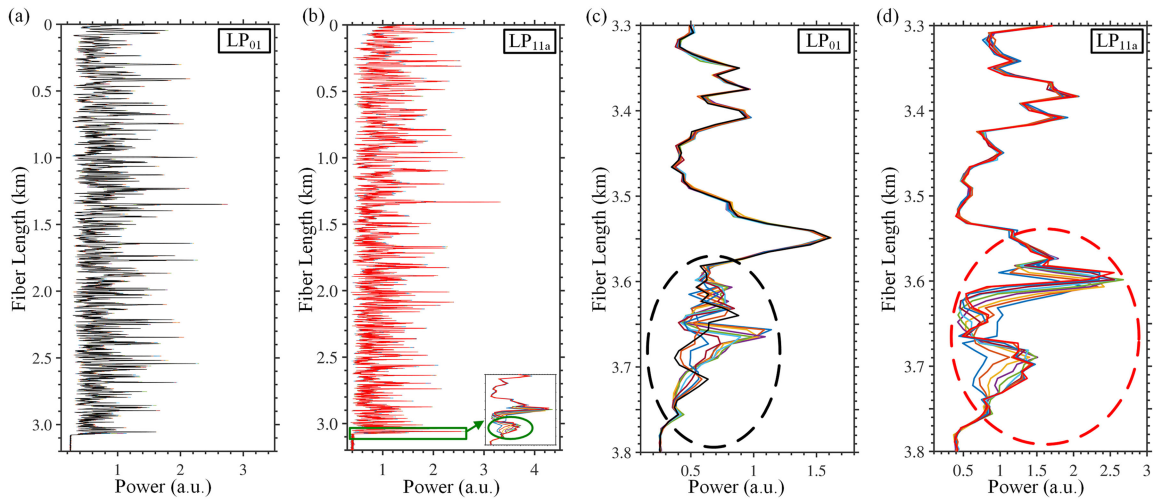


Fig. 3. 10 consecutive Rayleigh traces collected when injecting the LP<sub>01</sub> (a) and LP<sub>11a</sub> (b) mode into the TMF. Zoom-in images around the PZT location when injecting the LP<sub>01</sub> (c) and LP<sub>11a</sub> (d) into the TMF.

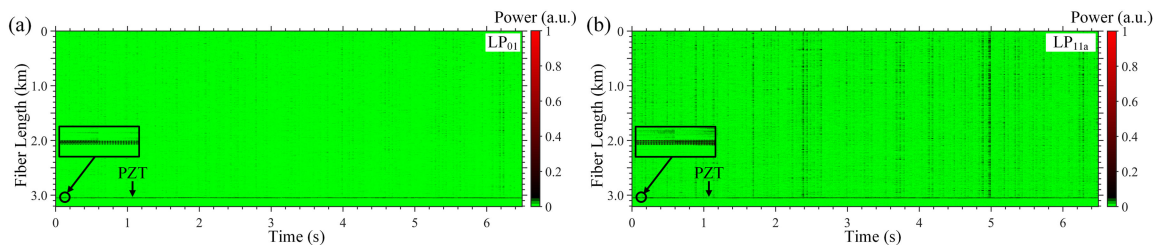


Fig. 4. Vibration position information associated with using the LP<sub>01</sub> (a) and LP<sub>11a</sub> (b) mode; Zoom-in images within 0.1 s at the PZT position (Insets).

collected when launching the LP<sub>01</sub> and LP<sub>11a</sub> mode, respectively. Zoom-in images of the Rayleigh traces around the PZT location are accordingly shown in the Figs. 3(c) and 3(d), when launching the LP<sub>01</sub> and LP<sub>11a</sub> mode. As marked with the dashed ovals in the zoom-in images, the PZT vibration clearly induces temporal power variations in the Rayleigh traces. Applying the time-domain differential method (i.e., subtracting the consecutive Rayleigh traces from the first reference one) [16], we can identify the location information of the PZT vibration event. Figs. 4(a) and 4(b) respectively represent the normalized absolute differential signals of the Rayleigh traces recorded when injecting the LP<sub>01</sub> and LP<sub>11a</sub> mode. The insets of Figs. 4(a) and 4(b) show zoom-in images within 0.1 s at the PZT position, as representative examples. The background noise of the LP<sub>11a</sub> mode is stronger than that of the LP<sub>01</sub> mode. This can be attributed to the fluctuations of the pulse power associated with the LP<sub>11a</sub> mode, as it propagates along the TMF. The intermodal coupling induced by the fan and that inevitably existed because of the index perturbations along the fiber created during the manufacturing process, both introduce power transfer mainly between the two degenerate modes (LP<sub>11a</sub> and LP<sub>11b</sub>). Fluctuations of the input pulse power are a main source of noise in optical fiber DAS system [21]. Additionally, injecting a mode into a FMF generates Rayleigh signals for the whole modes supported by the fiber [17]. Consequently, the intermodal coupling between the backscattered Rayleigh signals associated with the LP<sub>11a</sub> and LP<sub>11b</sub> mode is also considered another noise source, in Fig. 4(b). In contrast, the LP<sub>01</sub> mode generally provides less background noise because its intermodal coupling with the LP<sub>11</sub> mode is significantly mitigated, as shown in Figs. 2(a–d).

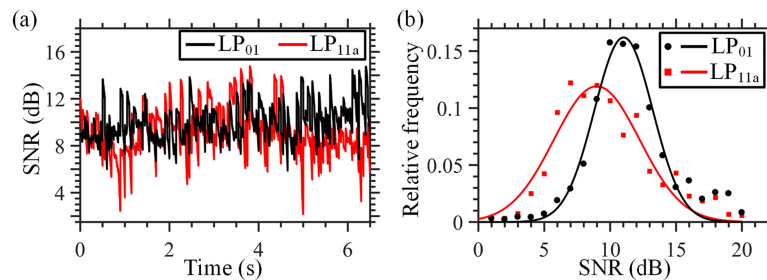


Fig. 5. (a) Change of the SNR values with time when injecting the LP<sub>01</sub> (black line) and LP<sub>11a</sub> (red line) mode, in the TMF. (b) Relative frequency histograms and fitted Gaussian distributions of the SNR values associated with the LP<sub>01</sub> (black line) and LP<sub>11a</sub> (red line) mode.

To quantify these observations, we calculate the SNR of the DAS defined as the ratio between the root-mean-square (RMS) of the differential signal at the PZT position and that of the remaining unperturbed fiber. The SNR is calculated over each periodic time of the 500 Hz PZT vibration event. The fluctuations of the SNR when injecting the LP<sub>01</sub> mode [Fig. 5(a), black line] occur because of the typical noise sources in the DAS (i.e., EDFA power changes, PZT cylinder instability, thermal noises, etc. [16]). On the other hand, the SNR of the LP<sub>11a</sub>-based DAS [Fig. 5(a), red line] exhibits similar fluctuations because of the common noises, but with additional dips in the SNR values found due to the intermodal coupling the LP<sub>11a</sub> mode encounters. Fig. 5(b) shows the relative frequency histograms of the SNR values for the LP<sub>01</sub> (black dots) and LP<sub>11a</sub> (red squares) mode, when choosing a 1 dB as a bin. The Gaussian distribution fit of the histogram has 11.02 dB mean and 2.22 dB standard deviation, for the SNR values of the LP<sub>01</sub> mode [Fig. 5(b), black line]. In contrast, the Gaussian distribution fit of the histogram has 8.98 dB mean and 3.26 dB standard deviation for the LP<sub>11a</sub> mode's SNR values [Fig. 5(b), red line]. These results conclude that the quasi-single-mode (QSM)-operated-TMF provides more reliable performance with higher SNR for the optical fiber DAS, compared with the case of using the LP<sub>11</sub> mode. For a FMF that supports propagating a larger number of modes, the non-degenerate LP modes would generally provide better performance for the DAS, compared with the case when injecting the degenerate modes.

The sensing results of the whole modes (LP<sub>01</sub>, LP<sub>11a</sub>, and LP<sub>11b</sub>) might be combined to improve the SNR of the FMF-based DAS system. However, the signal processing of this combination is relatively complicated and might not be feasible for real applications. Such analysis is out of the scope of this work because similar study was already implemented in Ref. [17].

### 3. Comparison Between the QSM-Operated-TMF and SMF for the DAS

We here compare the performance of the QSM-operated-TMF and SMF in the DAS system, when injecting optical pulses of various power levels. For simplicity, the LP<sub>01</sub> mode can be excited into the TMF by bypassing the photonic lantern, shown in Fig. 1(a), and directly aligning and joining the circulator's SMF and the TMF [22]. The injected pump power ( $P_{in}$ ) of an optical pulse in the DAS is limited by the nonlinearities of the used optical fiber. For meter-scale spatial resolution system, the fiber nonlinearity is dominant by the stimulated Raman scattering (SRS) which threshold power is directly proportional to the effective area of an optical fiber [11], [23]. For the fundamental mode, the effective areas of the used TMF and SMF are respectively  $130 \mu\text{m}^2$  and  $77 \mu\text{m}^2$ . As representative examples, Figs. 6(a)-6(c)/6(d)-6(f) each shows 10 consecutive Rayleigh traces when using the QSM-operated-TMF/SMF in the DAS system at  $P_{in}$  equals 0.47 W, 1.34 W, and 1.94 W, respectively. At 0.47 W and 1.34 W pump power, the QSM-operated-TMF maintains the speckles-profile of the Rayleigh traces along its length with negligible attenuation [Figs. 6(a) and 6(b)]. In contrast, when the pump power increases to 1.94 W, the Rayleigh signal of the QSM-operated-TMF gradually degrades with the fiber length [Fig. 6(c)]. This is to be expected because the SRS signal gradually builds up along the fiber length and becomes more obvious as increasing the pump power

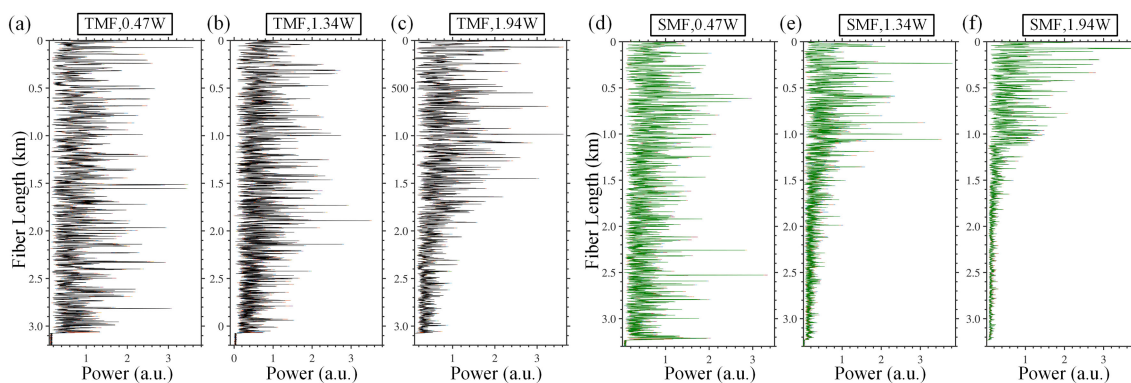


Fig. 6. 10 consecutive Rayleigh traces collected when using the QSM-operated-TMF/SMF at (a)/(d) 0.47 W, (b)/(e) 1.34 W, and (c)/(f) 1.94 W input power.

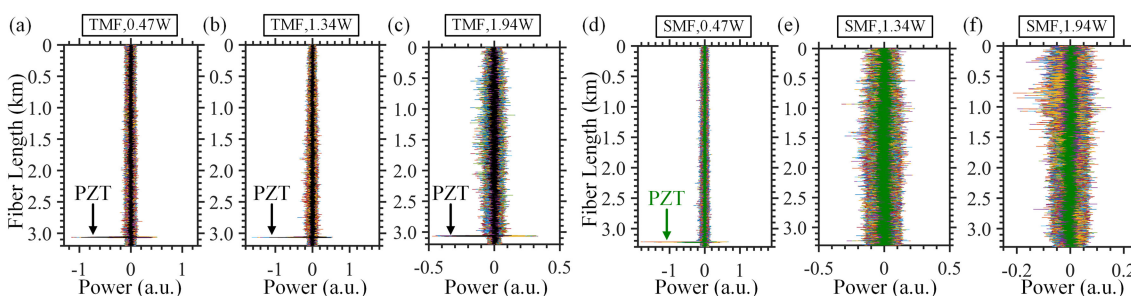


Fig. 7. Differential signals when using the QSM-operated-TMF/SMF at (a)/(d) 0.47 W, (b)/(e) 1.34 W, and (c)/(f) 1.94 W input power.

[24]. Compared with the QSM-operated-TMF, the SMF exhibits Rayleigh signal degradation along its length starting at lower pump powers. In particular, the SMF preserves the Rayleigh signal with negligible attenuation at 0.47 W pump power [Fig. 6(d)], while it significantly degrades the Rayleigh traces when  $P_{in}$  equals 1.34 W and 1.94 W [Figs. 6(e) and 6(f)].

Near the ends of the TMF and SMF, we attach 10 m sections of their lengths to the same PZT cylinder such that the two fibers are subjected to similar vibrations amplitude and frequency. As a representative example, we apply the differential method over 50 ms when the PZT is vibrating with 500 Hz frequency. The QSM-operated-TMF finds out the vibration location at the 0.47 W, 1.34 W, and 1.94 W input power as respectively shown in Figs. 7(a)–7(c). In good agreement with the results shown in Figs. 6(a)–6(c), the mean SNR of discovering the vibration location gradually degrades with increasing the input power level. In particular, the QSM-operated-TMF offers 11.56 dB, 10.27 dB, and 7.55 dB mean SNR at 0.47 W, 1.34 W, and 1.94 W input power, respectively. In contrast, the SMF recognizes the vibration location only at 0.47 W input power with 12.09 dB mean SNR [Fig. 7(d)], while it fails to find out the PZT position at 1.34 W, and 1.94 W [Fig. 7(e) and Fig. 7(f)]. Again, the behavior of the SMF for discovering the location of the PZT vibration event is consistent with its corresponding Rayleigh signals changes with the input power levels [Figs. 6(d)–6(f)]. Based on the results demonstrated in Figs. 6 and 7, one concludes that the QSM-operated-TMF is capable of designing a DAS with longer sensing range and higher spatial resolution, compared with the SMF-based DAS.

Another important point to explore is a comparison between the power levels of the Rayleigh signals collected when using the QSM-operated-TMF and SMF, under identical experimental conditions in terms of the gains of the EDFA1 and EDFA2. As aforementioned, we here bypass the photonic lantern when exciting the LP<sub>01</sub> mode in the TMF. We set the gain of the EDFA1 such

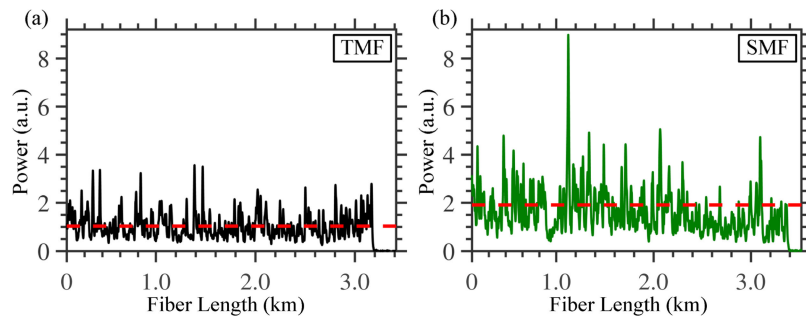


Fig. 8. Rayleigh traces collected when using the QSM-operated-TMF (a) and SMF (b), when fixing the gains of EDFA1 and EDFA2.

that both the QSM-operated-TMF and SMF work in the linear region and we adjust the gain of the EDFA2 to receive detectable Rayleigh signals from the both fibers. Fig. 8(a)/8(b) shows a Rayleigh trace recorded while employing the QSM-operated-TMF/SMF. It is worth confirming that the gain values of the EDFA1 and EDFA2 are kept constant while using the two fibers; therefore, the powers of the Rayleigh signals in Figs. 8(a) and 8(b) can be compared to each other. The corresponding mean power levels of the Rayleigh signals along the two fibers are labeled with the red dashed lines, as shown in Figs. 8(a) and 8(b). It is observed that the ratio of the mean power of the Rayleigh signal associated with the QSM-operated-TMF to that of the SMF is  $\sim 64.4\%$ . The power loss of the Rayleigh signal found when using the QSM-operated-TMF can be attributed to the core diameter mismatch between the circulator's SMF and TMF and/or avoiding collecting the Rayleigh signal of the  $LP_{11}$  mode, excited in the backward direction when launching the  $LP_{01}$  mode into the fiber.

To explore the main reason, we examine the first likely cause by launching two pulses with identical width and power into two separate fiber configurations: SMF of  $\sim 3.2$  km length and SMF-TMF-SMF where each SMF is  $\sim 1$  m long and the TMF is  $\sim 3.1$  km long. The power loss along the latter fiber configuration mimics the core diameter mismatch loss found in the QSM-operated-TMF-based DAS in both the pump and backward direction. We find that the power losses in the two fiber configurations are almost equal. This is likely because most of the intensity of the fundamental mode is concentrated around the fiber axis; therefore, the  $LP_{01}$  mode is transferred from the SMF/TMF to TMF/SMF with minor power losses. As a result, one can conclude that the power losses in the TMF-based DAS are primarily due to collecting only the Rayleigh signal of the  $LP_{01}$  mode. However, this is not considered a serious drawback for the QSM-operated-TMF-based DAS because this kind of power loss can be compensated with increasing the gain of the EDFA2 which enhances the signal along the entire fiber. In contrast, the Rayleigh power loss induced by the SMF nonlinearity [Figs. 6(e) and 6(f)] is difficult to be mitigated with the EDFA2. This is because when raising the gain of the EDFA2 to compensate the attenuation of the Rayleigh signal around the fiber end, the photodetector is saturated with the Rayleigh signal collected from the fiber portion near the input port.

It is worth mentioning that the speckle-like profiles of the Rayleigh traces, shown in Figs. 8(a) and 8(b), are formed because of coherent interference of the signals reflected by the fiber's scattering centers within the injected pulse duration [16]. Consequently, forming the shape of a Rayleigh trace is a random process and we are unable to control the positions of a Rayleigh trace's spikes/dips.

#### 4. QSM-Operated-TMF for Sensing Various Vibration Events

PZT cylinders are traditionally used to calibrate optical fiber DAS because its vibration amplitude and frequency can be well-controlled using a driving function generator. In this section, we show the ability of the QSM-operated-TMF-based DAS to detect other kinds of vibration events. As alternative



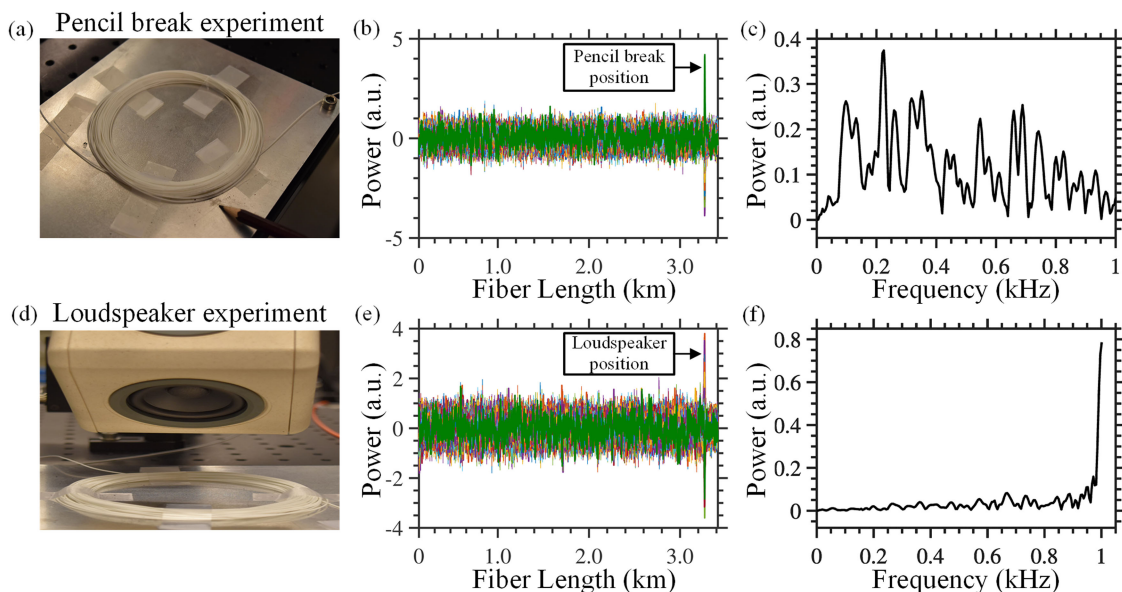


Fig. 9. Sensing the pencil break vibration event: (a) Experimental configuration of the TMF with the pencil. (b) Location information of the pencil break event, and (c) its corresponding power spectrum. Sensing the loudspeaker sound: (d) Experimental configuration of the TMF with the loudspeaker. (e) Location information of the loudspeaker sound, and (f) its corresponding power spectrum.

vibration sources, we particularly use a pencil break which mimics propagation and growth of cracks in civil construction [25] and a loudspeaker that transfers sound waves to the TMF through air. Since the vibration energies delivered to the TMF in these two scenarios are weaker than that delivered to the TMF through the direct contact with the PZT cylinder, we average every 10 Rayleigh traces to improve the SNR of the sensing system [25]. Near the TMF end, we use an adhesive tape to stick a 10 m long fiber loops to a 1 mm thick aluminum plate [Fig. 9(a)]. The pencil is broken at a point on the aluminum plate and next to the fiber loop circumference, as shown in Fig. 9(a). This experiment is important to verify the ability of using the QSM-operated-TMF-based in other real practical application, such as structural health monitoring. The pencil break vibration event includes broad frequency components (up to 5 MHz); however, this aluminum plate cannot vibrate beyond  $\sim 1$  kHz [25]. Fig. 9(b) shows the differential signals of the Rayleigh traces which clearly provide the position information of the pencil break event. The corresponding power spectrum of the pencil break event is exhibited in Fig. 9(c). Because of the upper limit of the aluminum plate vibrations frequency, we can only record partial frequency components.

When an acoustic wave is transmitted through air to meet an optical fiber, it impacts the fiber with small pressure, in comparison with vibrations delivered through metal or direct contact [26]. We here also try this challenge of sensing acoustic waves produced by a loudspeaker using the QSM-operated-TMF-based DAS. As shown in Fig. 9(d), we keep the 10 m TMF loops attached to the same 1 mm thick aluminum plate and we set the separation between the loudspeaker and the fiber to  $\sim 5$  cm. One advantage of the aluminum plate is it can absorb and convey more acoustic energy to the TMF. We adjust the loudspeaker to produce a monotone sound wave of 1 kHz frequency. The used loudspeaker has 10 W output power,  $8 \Omega$  electrical impedance, and 90 dB SNR. Figs. 9(e) and 9(f) show the position information of the loudspeaker vibration event and its corresponding power spectrum, respectively. Even when the acoustic wave is transferred through air, the QSM-operated-TMF-based DAS can efficiently extract the vibration information.

The sensing range of the designed TMF-based DAS can be extended to more than the  $\sim 3.1$  km, which is the length of the TMF we have. There are several techniques have been reported in the literature to improve the sensing range of optical fiber DAS [27], [28]. For example, combining the

OTDR and the optical frequency-domain reflectometry (OFDR) techniques results in designing an optical fiber DAS of 40 km sensing range [27]. Launching high-power pulses in the used optical fiber is a common factor to improve the sensing range of a DAS system. Consequently, including FMFs with the currently available DAS systems would improve their sensing range values.

## 5. Conclusion

We experimentally explore the performance of using a TMF in the DAS system when injecting the LP<sub>01</sub> and LP<sub>11</sub> mode under induced index perturbation. We find that the QSM-operated-TMF enhances the mean SNR of the DAS by 2.04 dB, compared with the case of injecting the LP<sub>11a</sub> mode into the TMF. Additionally, we compare the QSM-operated-TMF- and SMF-based DAS when launching optical pulses of different power levels. The QSM-operated-TMF-based DAS recognizes the vibration position of a PZT cylinder when using high input power levels (1.34 W and 1.94 W), while the SMF-based DAS fails to locate the PZT vibration event at the same input power values. Besides using the PZT cylinder as a vibration source, we show the ability of the QSM-operated-TMF-based DAS to efficiently calculate the positions and frequencies of vibrations produced by a pencil break event and a loudspeaker. The results of this work show the ability of designing an optical fiber DAS of longer sensing range and higher spatial resolution using the TMF, compared to the traditional SMF-based DAS.

---

## References

- [1] R. Ryf *et al.*, "Mode-division multiplexing over 96 km of few-mode fiber using coherent  $6 \times 6$  MIMO processing," *J. Light. Technol.*, vol. 30, no. 4, pp. 521–531, Feb. 2012.
- [2] E. Ip *et al.*, "SDM transmission of real-time 10 GbE traffic using commercial SFP + transceivers over 0.5 km elliptical-core few-mode fiber," *Opt. Exp.*, vol. 23, no. 13, pp. 17120–17126, 2015.
- [3] H. Huang *et al.*, "Mode division multiplexing using an orbital angular momentum mode sorter and MIMO-DSP over a graded-index few-mode optical fibre," *Sci. Rep.*, vol. 5, 2015, Art. no. 14931.
- [4] H. Wu *et al.*, "Few-mode fiber based distributed curvature sensor through quasi-single-mode Brillouin frequency shift," *Opt. Lett.*, vol. 41, no. 7, pp. 1514–1517, 2016.
- [5] A. Li, Y. Wang, and W. Shieh, "Few-mode fiber based optical sensors," in *Proc. IEEE Photon. Conf.*, 2015, vol. 23, pp. 319–320.
- [6] H. Z. Yang, M. M. Ali, M. R. Islam, K. S. Lim, D. S. Gunawardena, and H. Ahmad, "Cladless few mode fiber grating sensor for simultaneous refractive index and temperature measurement," *Sensors Actuators, A Phys.*, vol. 228, pp. 62–68, 2015.
- [7] J. Lim, Q. Yang, B. E. Jones, and P. R. Jackson, "Strain and temperature sensors using multimode optical fiber Bragg gratings and correlation signal processing," *IEEE Trans. Instrum. Meas.*, vol. 51, no. 4, pp. 622–627, Aug. 2002.
- [8] A. Sun and Z. Wu, "Multimode interference in single mode-multimode FBG for simultaneous measurement of strain and bending," *IEEE Sens. J.*, vol. 15, no. 6, pp. 3390–3394, Jun. 2015.
- [9] I. Ashry, A. Wang, and Y. Xu, "Mode-division-multiplexing of absorption-based fiber optical sensors," *Opt. Exp.*, vol. 24, no. 5, pp. 5186–5202, 2016.
- [10] I. Ashry, A. Wang, and Y. Xu, "Mode-based reconstruction of chemical distributions in optical fibers," *IEEE J. Sel. Topics Quantum Electron.*, vol. 23, no. 2, pp. 229–237, Mar./Apr. 2017.
- [11] M. Wang *et al.*, "Few-mode fiber based Raman distributed temperature sensing," *Opt. Exp.*, vol. 25, no. 5, pp. 4907–4916, 2017.
- [12] T. Yamate, G. Fujisawa, and T. Ikegami, "Optical sensors for the exploration of oil and gas," *J. Light. Technol.*, vol. 35, no. 16, pp. 3538–3545, Aug. 2017.
- [13] A. Barrias, J. R. Casas, and S. Villalba, "A review of distributed optical fiber sensors for civil engineering applications," *Sensors (Switzerland)*, vol. 16, no. 5, 2016, Art. no. 748.
- [14] Y. Weng, E. Ip, Z. Pan, and T. Wang, "Single-end simultaneous temperature and strain sensing techniques based on Brillouin optical time domain reflectometry in few-mode fibers," *Opt. Exp.*, vol. 23, no. 7, pp. 9024–9039, 2015.
- [15] H. Wu *et al.*, "Few-mode optical fiber based simultaneously distributed curvature and temperature sensing," *Opt. Exp.*, vol. 25, no. 11, pp. 12722–12732, 2017.
- [16] X. Bao, D. P. Zhou, C. Baker, and L. Chen, "Recent development in the distributed fiber optic acoustic and ultrasonic detection," *J. Light. Technol.*, vol. 35, no. 16, pp. 3256–3267, Aug. 2017.
- [17] M. Chen, A. Masoudi, F. Parmigiani, and G. Brambilla, "Distributed acoustic sensor based on a two-mode fiber," *Opt. Exp.*, vol. 26, no. 19, pp. 25399–25407, 2018.
- [18] Z. Qin, L. Chen, and X. Bao, "Wavelet denoising method for improving detection performance of distributed vibration sensor," *IEEE Photon. Technol. Lett.*, vol. 24, no. 7, pp. 542–544, Apr. 2012.
- [19] P. Sillard, M. Bigot-Astruc, and D. Molin, "Few-mode fibers for mode-division-multiplexed systems," *J. Light. Technol.*, vol. 32, no. 16, pp. 2824–2829, Aug. 2014.

- [20] P. Lu, I. Ashry, and Y. Xu, "Adaptive mode control for few-mode fiber based sensors and sensor networks," *J. Light. Technol.*, vol. 35, no. 16, pp. 3562–3568, Aug. 2017.
- [21] M. Ren, D.-P. Zhou, L. Chen, and X. Bao, "Influence of finite extinction ratio on performance of phase-sensitive optical time-domain reflectometry," *Opt. Exp.*, vol. 24, no. 12, pp. 13325–13333, 2016.
- [22] I. Ashry *et al.*, "Normalized differential method for improving the signal-to-noise ratio of a distributed acoustic sensor," *Appl. Opt.*, vol. 58, no. 18, pp. 4933–4938, 2019.
- [23] G. P. Agrawal, *Nonlinear Fiber Optics*, 3rd ed., Academic, 2001.
- [24] X. Sun, J. Li, and M. Hines, "SNR improvement in a Raman based distributed temperature sensing system using a stimulated Raman scattering filter," *Fiber Opt. Sensors Appl. XIV*, vol. 10208, 2017, Art. no. 102080E.
- [25] Y. Lu, T. Zhu, L. Chen, and X. Bao, "Distributed vibration sensor based on coherent detection of Phase-OTDR," *J. Light. Technol.*, vol. 28, no. 22, pp. 3243–3249, Nov. 2010.
- [26] Y. Wu, J. Gan, Q. Li, Z. Zhang, X. Heng, and Z. Yang, "Distributed fiber voice sensor based on phase-sensitive optical time-domain reflectometry," *IEEE Photon. J.*, vol. 7, no. 6, 2015, Art no. 6803810.
- [27] S. Wang, X. Fan, Q. Liu, and Z. He, "Distributed fiber-optic vibration sensing based on phase extraction from time-gated digital OFDR," *Opt. Exp.*, vol. 23, pp. 33301–33309, 2015.
- [28] F. Uyar, T. Onat, C. Unal, T. Kartaloglu, I. Ozdur, and E. Ozbay, "94.8 km-range direct detection fiber optic distributed acoustic sensor," in *Proc. Conf. Lasers Electro-Opt.*, 2019, pp. 1–2.